# Surface-Enhanced Raman Spectroscopy of Organic Molecules and Living Cells with Gold Plated Black Silicon

| | |
|---|---|
| Journal: | *ACS Applied Materials & Interfaces* |
| Manuscript ID | am-2020-13570w.R2 |
| Manuscript Type: | Article |
| Date Submitted by the Author: | n/a |
| Complete List of Authors: | Golubewa, Lena; State Research Institute Center for Physical Sciences and Technology; Belarusian State University Institute for Nuclear Problems<br>Karpicz, Renata; State Research Institute Center for Physical Sciences and Technology<br>Matulaitienė, Ieva; State Research Institute Center for Physical Sciences and Technology<br>Selskis, Algirdas; State Research Institute Center for Physical Sciences and Technology<br>Rutkauskas, Danielis; State Research Institute Center for Physical Sciences and Technology<br>Pushkarchuk, Aliaksandr; SSI Institute of Physical Organic Chemistry of the National Academy of Sciences of Belarus; Belarusian State University Institute for Nuclear Problems<br>Khlopina, Tatsiana; Belarusian State University Institute for Nuclear Problems<br>Michels, Dominik; King Abdullah University of Science and Technology Computer Electrical and Mathematical Science and Engineering Division<br>Lyakhov, Dmitry; King Abdullah University of Science and Technology Computer Electrical and Mathematical Science and Engineering Division<br>Kulahava, Tatsiana; Belarusian State University Institute for Nuclear Problems<br>Shah, Ali; Aalto University Department of Micro- and Nanosciences<br>Svirko, Yuri; University of Eastern Finland, Institute of Photonics<br>Kuzhir, Polina; University of Eastern Finland, Institute of Photonics; Belarusian State University Institute for Nuclear Problems |
| | |

# Surface-Enhanced Raman Spectroscopy of Organic Molecules and Living Cells with Gold Plated Black Silicon

*Lena Golubewa[1,2,]*, Renata Karpicz[1], Ieva Matulaitienė[1], Algirdas Selskis[1], Danielis Rutkauskas[1], Aliaksandr Pushkarchuk[3,2], Tatsiana Khlopina[2], Dominik Michels[4], Dmitry Lyakhov[4], Tatsiana Kulahava[2], Ali Shah[5], Yuri Svirko[6], Polina Kuzhir[6,2]*

[1] Center for Physical Sciences and Technology, Sauletekio Ave. 3, LT-10257 Vilnius, Lithuania

[2] Institute for Nuclear Problems, Belarusian State University, Bobruiskaya 11, 220030 Minsk, Belarus

[3] Institute of Physical Organic Chemistry, National Academy of Sciences of Belarus, Surganova 13, 220072 Minsk, Belarus

[4] Computer, Electrical and Mathematical Science and Engineering Division, 4700 King Abdullah University of Science and Technology, Thuwal 23955-6900, Saudi Arabia

[5] Department of Micro and Nanosciences, Aalto University, Espoo, P.O. Box 13500, FI-00076, Finland

[6] Institute of Photonics, University of Eastern Finland, Yliopistokatu 2, FI-80100 Joensuu, Finland

*Corresponding author: lena.golubewa@ftmc.lt

ABSTRACT

Black silicon (bSi) refers to an etched silicon surface comprising arrays of microcones that effectively suppress reflection from UV to near-infrared (NIR), while simultaneously enhancing the scattering and absorption of light. This makes bSi covered with an nm-thin layer of plasmonic metal, i.e. gold, an attractive substrate material for sensing of bio-macromolecules and living cells using surface-enhanced Raman spectroscopy (SERS). The performed Raman measurements accompanied with finite element numerical simulation and density functional theory analysis revealed that at the 785 nm excitation wavelength, the SERS enhancement factor of the bSi/Au substrate is as high as $10^8$ due to a combination of the electromagnetic and chemical mechanisms. This finding makes the SERS-active bSi/Au substrate suitable for detecting trace amounts of organic molecules. We demonstrate the outstanding performance of this substrate by highly sensitive and specific detection of a small organic molecule of 4-mercaptobenzoic acid and living C6 rat glioma cells nucleic acids/proteins/lipids. Specifically, the bSi/Au SERS-active substrate offers a unique opportunity to investigate the living cells' malignant transformation using characteristics protein disulfide Raman bands as a marker. Our findings evidence that bSi/Au provides a pathway to the highly sensitive and selective, scalable, and low-cost substrate for the lab-on-a-chip SERS biosensors that can be integrated into silicon-based photonics device.

KEYWORDS

Black silicon, surface-enhanced Raman spectroscopy, enhancement factor, DFT, small organic molecules, living cells.

## INTRODUCTION

Curing neurodegenerative diseases and stem cell therapies require effective biosensors for real-time *in vivo* controlling and monitoring the growth and functional activity of the cells. Materials used for biosensor systems must provide cellular viability and stable functional state, preserve sterility and preferably be compatible with silicon photonics to address the lab-on-chip technological flow[1].

Raman spectroscopy is actively implemented in biosensing[2] partially because it can use NIR radiation, which is less damaging for biological tissues providing deeper – in comparison with VIS light – tissue penetration[3]. In addition, detecting NIR radiation does not require any specific sample preparation keeping the object unaltered[4]. The sensitivity and specificity of Raman measurements can be drastically improved by using substrates enabling the surface-enhanced Raman scattering spectroscopy (SERS). This technique allows one to detect low bio-molecules concentrations[5,6,7] changes in cell metabolism[8] or cells viability[9], discriminate individual vesicles[10] as well as to real-time control of biochemical changes[11,12,13] by using so-called SERS-active substrates, which conventionally based on noble metal (Au, Ag, Cu) nanostructures[14,15,16]. They allow enhancement of the Raman signal due to the surface plasmon resonance, associated with the collective motion of the conductive electrons in the vicinity of "hot spots" at high curvature metal structures[17]. This makes SERS signal very sensitive to the substrate morphology[18] and requires fabrication techniques providing fine control over the geometry and size of nanostructures/hot spots[19], which should be uniformly distributed over the entire substrate to be employed for biosensing.

Although SERS-active substrates based on the metal micro- and nanostructures deposited on the glass are widely available on the market[20], their performance is often limited by low curvature of metal nanoparticles and/or small surface density of the hotspots, that do not allow analytes'

detection at concentrations at the ppb level[21]. To improve the sensitivity, we suggest employing in SERS the substrates based on the black silicon (bSi), which has been proposed in 1997 to increase absorbance and suppress reflectivity of the silicon[22] by forming cone-shaped structures of micrometers height over the sample surface[23]. These properties made bSi a versatile material for various applications, such as solar cells[24], THz emission sources[25], microfluidic devices[26], chemical[27], and biological sensors[28], antibacterial surfaces[29,30], etc.

BSi forms a functional platform for the fabrication of SERS active substrates because the apexes of the high curvature cone-like structures can serve as active sites for electromagnetic field (E-field) enhancement. Its performance in SERS has been demonstrated with high-intensity 532 nm laser by detecting individual algal cell (*Chlorella vulgaris*)[31] on bSi substrates covered with 200-400 nm thick gold layer[31,32]. Unfortunately, the hundreds-nm-thick Au film smooths out the curvature of the bSi cones suppressing significantly the Raman signal enhancement.

*In vivo* bSi based SERS biosensing challenges the excitation of Raman signal with low power NIR lasers, i.e. decrease of laser power and increase of enhancement factor (EF) are needed. The latter implies decreasing the thickness of the gold layer to be deposited on the bSi and increasing the number of hot spots at needles' apexes.

The electromagnetic field enhancement at the metal surface may originate from the electromagnetic (EM) and chemical (CM) mechanisms[33]. The EM mechanism occurs when the analyte molecule is situated in the close vicinity of the hot spots on the substrate surface. Since the induced dipole moment of the molecule is proportional to the electric field, it drastically increases at the plasmon resonance. Moreover, the electromagnetic wave emitted by the analyte at the shifted frequency also enhances due to the plasmonic effect. As a result, the Raman signal is proportional to the fourth power of the local field enhancement factor (EF)[34].

The chemical (also referred to as the charge transfer) mechanism occurs when the studied substance forms chemical bonds with the material of the substrate. These bonds lead to the increase of the polarizability and, as a consequence, the intensity of Raman scattering.

Understanding of the mechanisms of E-field enhancement in the bSi/Au system will make it possible to predict the EF, which also depend on the morphology of the bSi surface (cones height and base diameter, the density of the cones) and the gold layer thickness.

In this paper, we propose effective, non-invasive, label-free, high-speed SERS detection of trace amount of small organic molecules and living rat glioma cells C6 utilizing bSi covered with 25÷50 nm gold layer. Using finite elements method (FEM) and density functional theory (DFT) we also perform numerical modeling and theoretical analysis of the SERS signal of organic molecules/cells deposited on bSi/Au substrate and reveal contributions of EM and CM mechanisms in the E-field enhancement. The obtained results allow us to reveal the optimal morphology and composition of the bSi/Au SERS-active substrate for *in vivo* biosensing of trace amounts of biomolecules and living cells.

## RESULTS AND DISCUSSION

### *Experimental results*

Scanning electron microscope (SEM) images of bSi and bSi/Au are presented in Fig. 1, (a,b) and (c,d), respectively. Figure 1e shows the transmission electron microscopy (TEM) image of an individual silicon cone covered with the golden layer. One can observe that substrates consist of vertically oriented quasi-regular cone-like structures. The height and a base diameter of cones comprising a bare bSi substrate are 495±19 nm and 221±24 nm, respectively, while the apex curvature radius is 26±4 nm (Fig. 1, b). On the bSi/Au substrates, the height of the cones is 497±21 nm at the apex curvature radius of 36±5 nm. It is worth noting that the roughness of the gold layer

is as high as 10-50 nm (Fig. 1, d) due to nanoscale irregularities and nano-roughness of the bSi cones. The average thickness of the deposited gold layer was 25÷50 nm. The Au semispheres on the bSi substrate vary in size and separation distance. For this reason, we analyzed the distribution of the particle sizes from the SEM image of the $SiO_2$/Au surface. SEM image of the $SiO_2$/Au is presented in Fig. 1S (Supplementary Information). This surface was obtained in the same conditions as the surface of bSi/Au, but is much easier for analysis. It consists of the hemisphere structures; their diameter distribution is presented in Fig. 1S, b. As the conditions were the same both for bSi and $SiO_2$ we used $SiO_2$/Au SEM image to obtain nanoparticles size distribution assuming that the Au structures on the $SiO_2$ and bSi would be very similar. Since hemispheres with the diameters in the range from 40 to 60 nm (almost 70% of all hemispheres) give the major contribution to the SERS enhancement, for further simulations we assumed that studied nanoparticles have a diameter of 50 nm.

The effective surface area of the bSi substrate is about 2.4 times larger than that of the flat $SiO_2$ substrate, which was confirmed by the AFM method earlier (see [35]). The presence of semispherical structures on an inclined lateral surface does not allow the cantilever to correctly repeat the surface profile and introduces additional errors in measurements. But assuming that Au roughness on the flat $SiO_2$ and on the conical Si surface is of the same order (the conditions of Au deposition were the same), it will add the same multiplier to the values of both surface areas, thus bSi/Au to $SiO_2$/Au surfaces ratio could be estimated to be also about 2.4.

To quantitatively evaluate the performance of the bSi/Au SERS-active substrate we employ 4-mercaptobenzoic acid (4-MBA) molecule with a well-known Raman spectrum. When 4-MBA molecules are deposited on the gold plated substrate, the nearest to the substrate molecules form covalent bonds with the gold through S-H groups. That is by washing the sample in the ethanol

one can remove the non-bunded molecules and obtain a monolayer of 4-MBA molecules covalently bonded to the substrate.

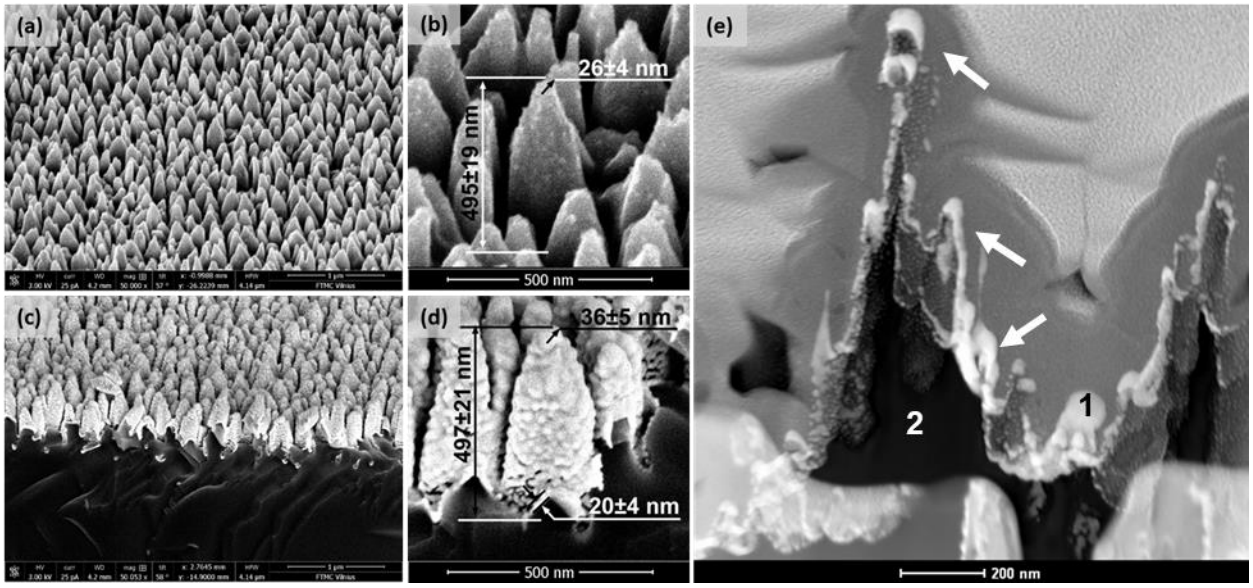


**Figure 1.** SEM images of bSi (a, b) and bSi/Au (c, d) substrates; (e) TEM image of the silicon cone covered by 25-50 nm thick gold layer. Gold structures on the bSi substrate are marked with arrows. White color corresponds to Au components (1), dark grey area corresponds to Si (2)

Raman spectra of 4-MBA molecule monolayer deposited on $SiO_2$/Au and bSi/Au substrates are presented in Fig. 2 (a) and Fig. 2 (c) respectively. At the same measurement conditions (10 μW, 30 s accumulation time) 4-MBA bands are no detectable when the molecule monolayer is deposited on the plane $SiO_2$/Au substrate, while these bands are clearly resolved for 4-MBA monolayer deposited on the bSi/Au surface. All observed bands are in good correspondence with the Raman spectrum of the bulk 4-MBA (Fig. 2b) described elsewhere [33, 36].

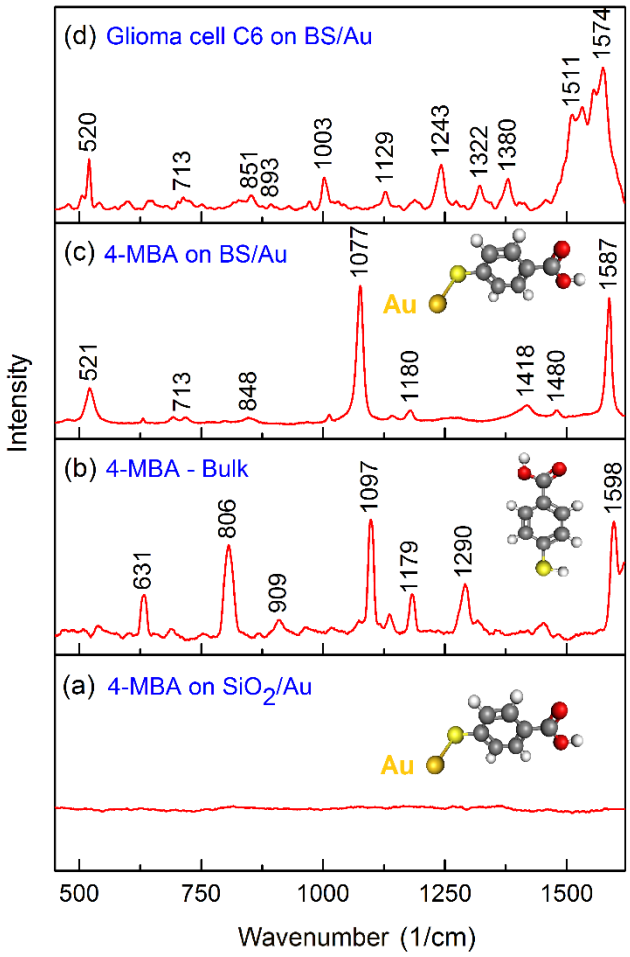


**Figure 2.** Comparison of Raman spectra of 4-MBA monolayer on $SiO_2$/Au smooth substrate (a), of bulk 4-MBA (b), and SERS spectra of 4-MBA (c) and living rat glioma cell (d) on the bSi/Au substrate. The spectrum of a living cell was recorded in aqueous Hepes-buffer solution. Buffer spectrum was subtracted from living cells Raman spectra. The excitation wavelength is 785 nm.

It is worth noting that the S-H stretching mode of 4-MBA at about 2570 $cm^{-1}$, typical for a Raman spectrum of bulk 4-MBA, is absent in the Raman spectrum of the monolayer (data are not shown) because this resonance is suppressed by the covalent bond, which S-H group forms with the gold layer.

The enhancement factor of the SERS-active bSi/Au substrate can be found from the following equation[37]:

$$EF = \frac{I_{bSi/Au}/N_{bSi/Au}}{I_{bulk}/N_{bulk}} \quad , \qquad (1)$$

where $I_{bSi/Au}$ ($N_{bSi/Au}$) and $I_{bulk}$ ($N_{bulk}$) are Raman intensities (numbers of irradiated molecules) of 4-MBA monolayer on the bSi/Au substrate and bulk 4-MBA on the $SiO_2$ substrate obtained at the same laser power and time accumulation, respectively. In our experimental conditions, the laser spot area on the bSi/Au substrate was 1.28 μm$^2$, however atomic force microscopy measurements indicated that the effective surface area of the bSi/Au substrate is 2.4 times larger, i.e. it is equal to 3.07 μm$^2$. That is at the surface density of 0.5nmol/cm$^2$, [37] the number of adsorbed molecules on the bSi/Au substrate is $N_{bSi/Au} = 9.2 \times 10^6$ . Since the penetration depth of the laser radiation into the bulk 4-MBA sample is about 10 μm and the molecular density 1.5 g/cm$^3$, the number of molecules in the irradiated volume is $N_{bulk} = 7.5 \times 10^{10}$. Therefore at the measured intensity radio of $I_{bSi/Au}/I_{bulk} = 2.3 \times 10^5$ for the $\nu_{12}$ ($a_1$) aromatic ring breathing mode at 1077 cm$^{-1}$ , Eq.(1) gives the SERS enhancement factor $EF \approx 2 \times 10^8$.

From the top-down SEM images of bSi/Au substrate (see Fig. 3, a) one can see very good structural uniformity of the substrate. This suggests that bSi/Au substrates exhibit good SERS signal uniformity over large areas. In Fig. 3, b SERS mapping of the substrates with 4-MBA monolayer in 3 randomly selected 10×10 μm areas with 1μm resolution are performed. Images are reconstructed using a 1077 cm$^{-1}$ band in 4-MBA SERS-spectrum. Equal SERS-signal intensities indicate very good uniformity over the whole sample area.

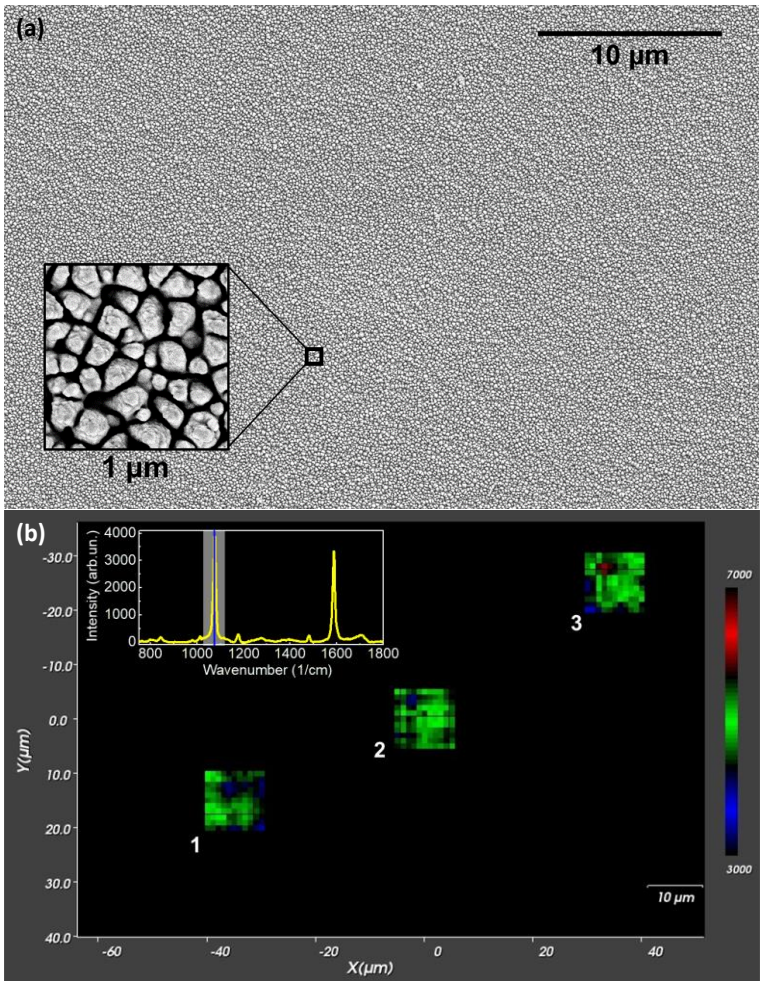


**Figure 3.** Uniformity of bSi/Au SERS substrate. (a) – Top-down SEM image of bSi/Au substrate, inset gives 1×1 µm area. (b) – Map of the background-corrected Raman intensity. 1077 $cm^{-1}$ C–S stretch vibration peak, a 50× objective (NA 1.0) were used. The map resolution is 1 µm. 1,2,3 – separate 10×10 µm maps taken randomly from a 75×115 µm area. Inset gives a SERS spectrum of 4-MBA monolayer from 1×1 µm pixel.

Experimental determination of 4-MBA SERS spectra stability on the bSi/Au substrate over a long time period was performed (see Supplementary Information Fig. 2S). Measurement of the SERS spectrum of 4-MBA molecules was repeated in 8 months. Both spectra (initial and after 8 months of storing in the air) demonstrate the same intensities for the same samples, performed

with identical conditions for SERS spectrum registration. Some changes in the positions of the bands indicate probable changes due to storage in air (strengthening of the C=O band (1706 $cm^{-1}$)), however, these changes do not affect the SERS substrate efficiency. Moreover, data presented in Fig. 3S (Supplementary Information) indicate, that bSi/Au substrate provides a possibility to obtain SERS spectra of 4-MBA molecule with extremely low laser power (two spectra for comparison – 0.5 mW and 1 μW).

SERS-active substrates (for instance, silicon Ag-capped Si nanopillar systems [38]), are often hydrophobic, which limits their use for the detection of organic molecules, cellular structures, or the cells themselves in aqueous media. The hydrophobicity of these structures is a consequence of the nanostructured nature of the substrate. In contrast, BSi substrates exhibit very nice adhesive properties, similar to the commercially provided tissue-treated plastics for cell culture [39]. Due to a combination of micro- and nanoroughnesses bSi substrates are hydrophilic (see Supplementary Information, Fig. 4S Water-drop hydrophilicity assay of bSi/Au and plastic (Nunc)) and therefore biocompatible. Hydrophilicity, adhesion, and SERS-activity provide a tremendous advantage of the bSi/Au substrates over the existing once in biochemical, biological, and biomedical applications, which implies working in aqueous environments.

The large enhancement factor allows us to employ the bSi/Au SERS-active substrate for the detection of the living C6 rat glioma cells. Using Propidium Iodide (PI) assay, it was shown that the cells on the bSi/Au substrate were viable, preserved their usual morphology, and formed a good monolayer (see Fig. 5S, Supplementary Information).

Measurements of a living cell are complicated by continuous cell “movement” due to the dynamics of biochemical reactions taking place inside the cell and due to the constant medium convective flow, which cannot be fully avoided despite the low laser power and relatively short

signal accumulation time. These factors led to some changes in SERS spectra bands intensities demonstrating high dynamics of intracellular processes. For instance, one can observe from Fig. 4 that the intensity of the $CH_3$ symmetric stretch band at 1380 $cm^{-1}$ varies slightly from measurement to measurement due to the density fluctuations in the vicinity of the hot spots on the bSi/Au substrate. Thus, the cellular activity imposes stringent requirements on biosensors' substrates being developed for biosensors. These include a uniform and dense hot spot distribution and a high enhancement factor that will enable real-time monitoring of the cell activity with high accuracy and about one-micron spatial resolution.

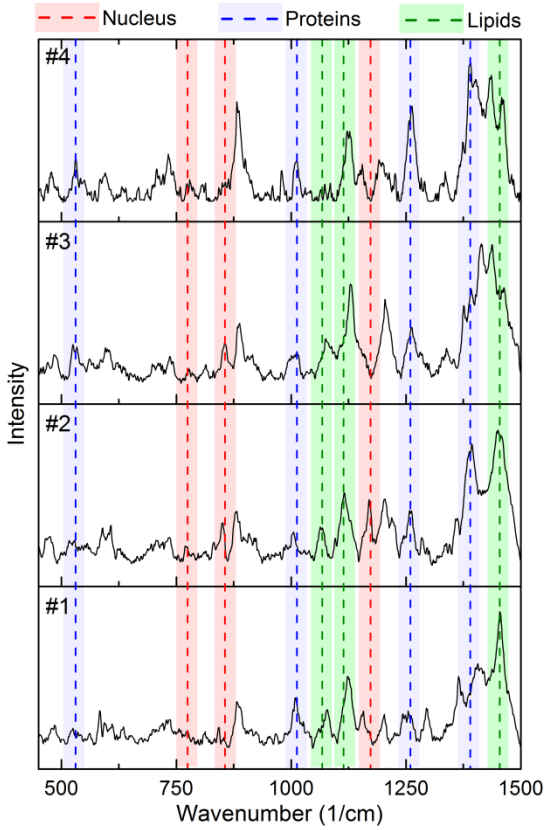

**Figure 4.** SERS spectra of a living rat glioma cell on the bSi/Au substrate, measured at one point in one-minute intervals. Specific markers indicate the intensity changes of some characteristic bands.

In the present study, we investigate the living cells by averaging five separate Raman spectra measured at the same point. The typical averaged spectrum of a living rat glioma cell C6 on the bSi/Au substrate is presented in Fig. 2d. Similar to 4-MBA monolayer (see Fig 2a), we do not observe Raman bands of living cells seeded on the reference $SiO_2$/Au substrate.

Specific bands of bio-macromolecules of C6 glioma cells, detected in the "fingerprint" spectral region, are grouped and summarized in Table 1. Averaging makes Raman spectra poorly suited to identify specific molecules in living cells such as specific proteins or lipids[40], but they can serve to detect relative concentration changes of bio-molecules. By using bSi/Au substrate we managed to resolve the characteristic bands of nucleic acids, proteins, and lipids. This makes it possible to distinguish between normal and cancerous cells by taking into account the higher relative content of nucleic acids specific to malignant cells transformation[41,42]. Specifically, relatively high intensities of 787 $cm^{-1}$ (U, C, T, O-P-O symmetric stretch), 827 $cm^{-1}$ (O-P-O), 1322 $cm^{-1}$ and 1574 $cm^{-1}$ (A, G) bands indicate the high content of nucleic acids characteristic for cancer cells; strong bands at 1243 $cm^{-1}$, 1273 $cm^{-1}$, 1288 $cm^{-1}$ correspond to the bands of Amide III giving information on the secondary structure of proteins (1243 for β-sheet and 1288 for α-helix); high intensity of 506 $m^{-1}$, 520 $cm^{-1}$ and 540 $cm^{-1}$ reveals high content of proteins with disulfide bonds enriched with cysteine. Main intracellular function of such proteins in cells is the participation in redox reactions and regulation of intracellular balance between oxidants and reductants. One of the key player in the redox balance in cells is the glutathione/glutathione-disulfide (GSH/GSSG) ratio. It has been shown[43] that decreased GSH/GSSG ratio (increased GSSG fraction) is the key factor in cancer

progression. Thus, bSi/Au SERS-active substrates offer unique opportunity to investigate the cells malignant transformation using characteristic protein disulfide Raman bands as a marker.

Nevertheless, we should admit, that the SERS effect depends on the distance and therefore it is really possible to obtain SERS signal only from the attached to the substrate part of the cell. BSi/Au substrate is biocompatible and exhibits nice adhesive properties (as it was demonstrated previously). It was shown that cell/substrate distance varies from 10 to 80 nm [44] for most parts of the cells and 25 ± 10 nm for peripheral lamellipodia [45]. This explains the fact that the majority of detected lines belong to lipid structures (see Table 1), nevertheless proteins and DNA from the adjacent to the membrane organelles are also observed.

SERS spectra of C6 glioma cells do not exhibit strong lines of Amide I, but nevertheless, it is supposed, that there is some weak impact of α-helix at ~ 1645 $cm^{-1}$ in the whole spectrum. Amide I is very active and useful for IR measurements as these bands are strong, but in Raman Amide I is not so significant and even was shown to be suppressed in SERS and TERS of protein specimens [46]. Moreover, due to the distance dependence of the signal enhancement in SERS spectra, we obtain information mainly on the cell membrane, which is closely located to the SERS substrate, and some structures adjacent to the membrane. Thus, protein impact in the SERS signal is visualized by Amide III, which is more active in Raman and there is no overlap with the bands of lipids and nuclear structures.

**Table 1.** The major peaks location in a "fingerprint" region of Raman spectra of main biomacromolecules, SERS spectrum of C6 rat glioma cells, and their assignments (Raman spectra band locations and their assignments are taken from [40])

| | Raman spectrum peaks location ($cm^{-1}$) | SERS spectrum peaks location ($cm^{-1}$) for C6 rat glioma cells | Peak assignments |
|---|---|---|---|
| Nucleic acids | 723-728 | 727 | C-N head group in Adenine |
| | 763 | 768 | Pyrimidines (Cytosine, Thymine, Uracil) |
| | 782-792 | 787 | Uracil, Cytosine, Thymine ring breathing; O-P-O symmetric stretch |
| | 813 | 817 | RNA, A-type DNA |
| | 828 | 827 | O-P-O |
| | 898 | 894 | Adenine, nucleotide backbone |
| | 1084-1095 | 1088, 1097 | PO2 stretch |
| | 1173-1180 | 1180, 1188 | Cytosine, Guanine, Adenine |
| | 1304-1342 | 1322, 1342 | Adenine, Guanine |
| | 1487 | 1484 | Guanine, Adenine |
| | 1510 | 1509 | Adenine |
| | 1578 | 1574 | Guanine, Adenine |
| Proteins | 500-550 | 506, 520, 540 | Disulfide S-S stretch (conformation dependent) |
| | 755-760 | 753 | Trp ring br. |
| | 850-855 | 852 | Pro C-C stretch (Collagen); Tyrosine ring br. |
| | 935-937 | 930 | Pro C-C stretch (Collagen); C-C backbone stretch (α-helix) |
| | 1000-1006 | 1003 | Phe symmetric ring br. |
| | 1014 | 1018 | Trp symmetric ring br. |
| | 1030-1033 | 1032 | Phe C-H in-plane bend |
| | 1066; 1080-1083; 1125-1128 | 1069, 1128 | C-N stretch |
| | 1155-1158 | 1155 | C-C/C-N stretch |
| | 1225-1280 | 1243, 1273, 1288 | Amide III (random coil 1225-1240; β-pleated sheet 1240-1260; α-helix 1260-1300) |
| | 1600-1610 | 1600, 1610 | Phe, Tyr C=C in-plane bending |
| Lipids | 719 | 714 | CN+C (choline) |

| | | | |
|---|---|---|---|
| | 955-975 | 953, 961, 972 | $CH_3$ deformations |
| | 1030-1130 | 1042, 1110 | skeletal C-C stretches (cis 1030-1040; chain trans 1055-1066;<br><br>chain random 1080-1085; chain 1092-1098; trans 1127) |
| | 1365-1380 | 1380 | $CH_3$ symmetric stretch |
| | 1440-1460 | 1437, 1457 | $CH_2$ scissors |

*Finite elements method: electromagnetic enhancement contribution to SERS*

We performed 3D FEM modeling of the interaction of the light wave propagating along the substrate normal with the cone-like Si structures covered by the 20-50 nm thick gold layer. By analyzing the SEM and TEM images we found that the gold layer can be presented as an ensemble of spheres, bi-spheres, and dumbbell-like particles having a different orientation to the cone axis (see Fig. 5). We also took into account that nanoparticles may have different sizes and compositions.

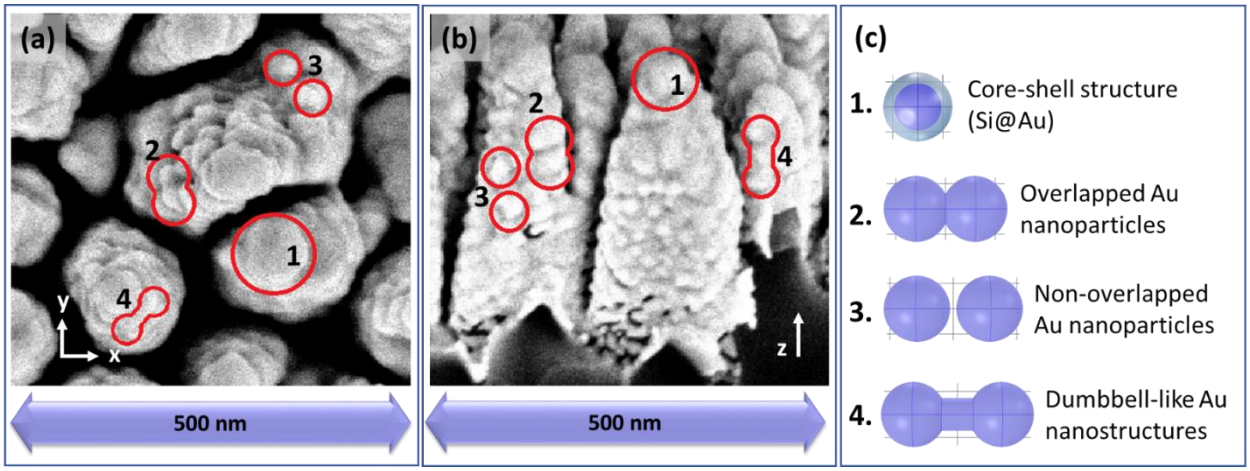


**Figure 5.** (a) top-view SEM image of bSi/Au showing horizontally (perpendicular to the wavevector $\vec{k}$) oriented bi-spheres and dumbbell-like particles; (b) side-view SEM image of bSi/Au showing vertically (along the wavevector $\vec{k}$) oriented bi-spheres and dumbbell-like particles; (c) elementary nanostructures selected for numerical simulation of the E-field enhancement.

We assume that the nanoparticles were irradiated with a plane electromagnetic wave and consider the complex refractive indices of nanoparticles' materials dependent on the wavelength. Au dielectric properties in the optical and (IR) frequency ranges were simulated by COMSOL Multiphysics via the Drude model taking into account the experimental data presented in [47] and

the fact that the wavelength of the incident radiation is much larger than the characteristic nanoparticles mean size and golden layer thickness. The bSi/Au cone edge was modeled by a spherical particle of the core-shell Si@Au type. From SEM images presented in Fig. 1 we reveal that the radius of the Si core and thickness of the gold shell varies in the 36÷44nm and 13÷21nm ranges, respectively.

The numerical simulation showed that there are three absorption bands (see Fig. 6). The band in the NIR region dominates having the central wavelength depending on the Si core radius and Au shell thickness. The bigger the Si core radius, the higher the absorption cross-section, and the longer the central wavelength (Fig. 6, a). The decrease of the Au layer thickness also leads to the red-shift of the absorption band, but the absorption cross-section maximum decreases (Fig. 6, b).

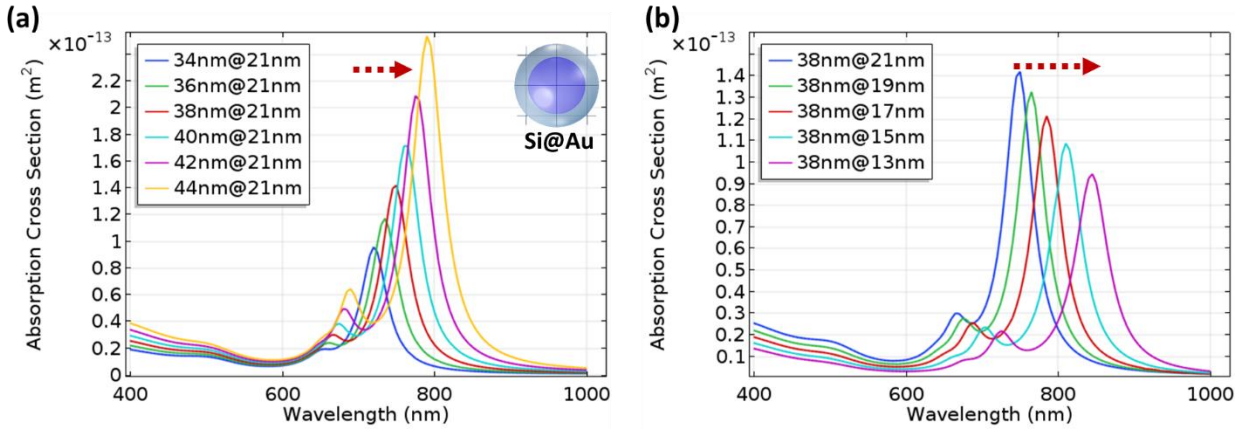


**Figure 6.** Absorption cross-section as a function of wavelength simulated for Si@Au spherical nanoparticle. (a) changing Si-core radius from 34 nm to 44 nm at Au-shell thickness of 21 nm, (b) changing Au-shell thickness from 13 nm to 21 nm at a Si-core radius of 38 nm.

Simulation results strongly support the hypothesis that in the red-NIR spectrum region, the absorption resonance of a gold bi-sphere depends not only on the distance between the sphere centers and nano-gap sizes but also on the orientation of the pair to the EM wave propagation

direction (Fig. 7). If bi-spheres are oriented along the wave vector $\vec{k}$ of the EM wave, then there is a strong NIR absorption band, which is absent in the individual Au nanospheres. Red absorption maximum arises from the nano-gaps in overlapped structures and is red-shifted with the increase of the distance between the spheres (Fig. 7, a).

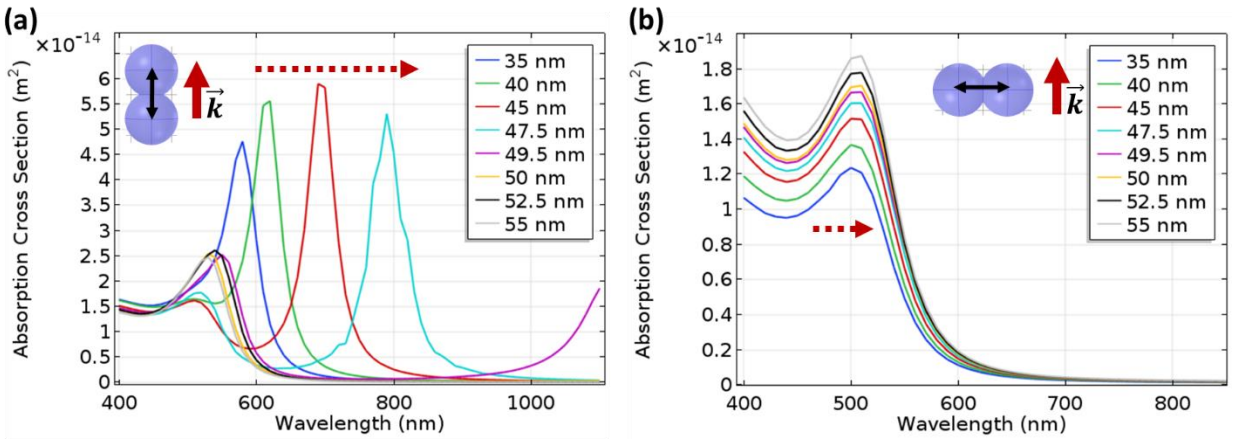


**Figure 7.** Absorption cross-section as a function of the wavelength of the Au bi-spheres (r=25 nm) having distances between the sphere centers from 35 nm (overlapped spheres) to 55 nm (non-overlapped spheres). The electromagnetic wave propagates (a) along and (b) perpendicular to the bi-sphere axis.

If the bi-sphere axis is oriented perpendicular to $\vec{k}$ (i.e. horizontally), then a green resonance peak characteristic to gold nanostructures appears. The central position of this band "floats" in the 500-515 nm range when the distance between the centers of spheres changes, however, there is no absorption resonance in red or NIR spectrum range (Fig. 7, b).

The system of non-overlapped Au spheres was further modified into a dumbbell-like structure, which well model Au droplets on the Au layer. A bridge between the two spheres led to the appearance of an additional absorption peak, which red-shifts with the increase of the distance between the spheres (Fig. 8, a) and disappears for non-overlapped Au spheres (Fig. 8, b). For non-

overlapped Au spheres "green" absorption maximum blue-shifts with the increase in the distance between the sphere centers (Fig. 8, b) approaching the plasmon resonance of the individual Au nanoparticle at 560 nm.

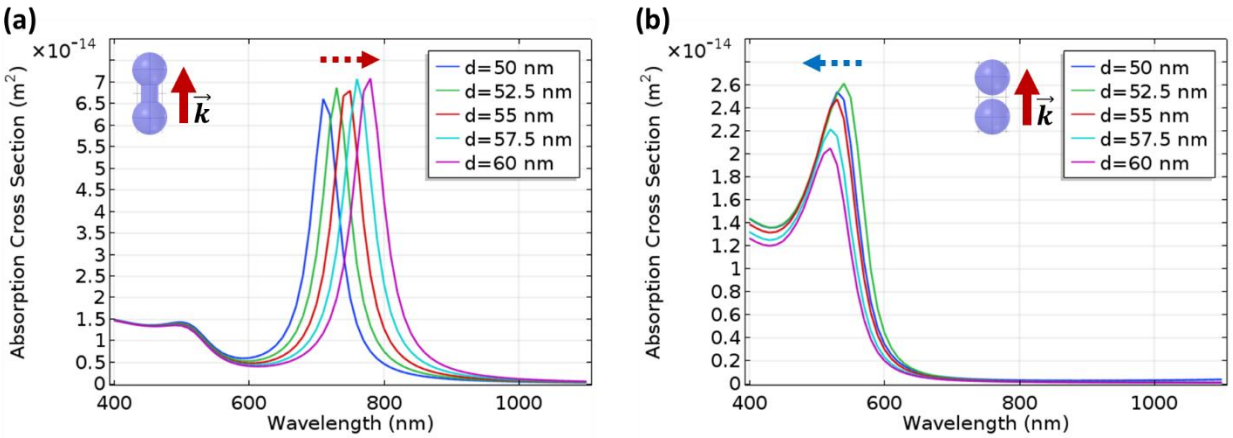


**Figure 8.** Absorption cross-section as a function of wavelength, simulated for (a) Au dumbbell-like nanoparticle (r=25 nm) and (b) Au bi-spheres with different distances between the sphere centers. The electromagnetic wave propagates along the bi-sphere axis, d is the distance between the sphere centers.

Figure 9 presents the numerical simulation of the E-field enhancement in nanostructures having an absorption maximum at 785 nm. For Si@Au (44nm@21nm) nanoparticle with the absorption maximum of 785nm, the E-filed enhancement on the outer Au surface is as high as 20 (Fig. 9, a) giving EF ≈ $1.6\times10^5$. In the overlapped Au nano-spheres (Fig. 9, b), there exists a 70-fold E-field enhancement in the nano-gaps between the overlapped spheres (EF ≈ $2.4\times10^7$). E-field enhancement on the sphere surface gives EF equal to approximately $10^4 \div 10^5$. For non-overlapped Au spheres, the E-field enhancement occurs only in the gap between the spheres with EF of the order of $10^4$ (Fig. 9, c). But for the refined model on the Au dumbbell structure E-field

enhancement occurs over the whole structure surface, but the most significant E-field enhancement in the space between is as high as $10^5$ (Fig. 9, d).

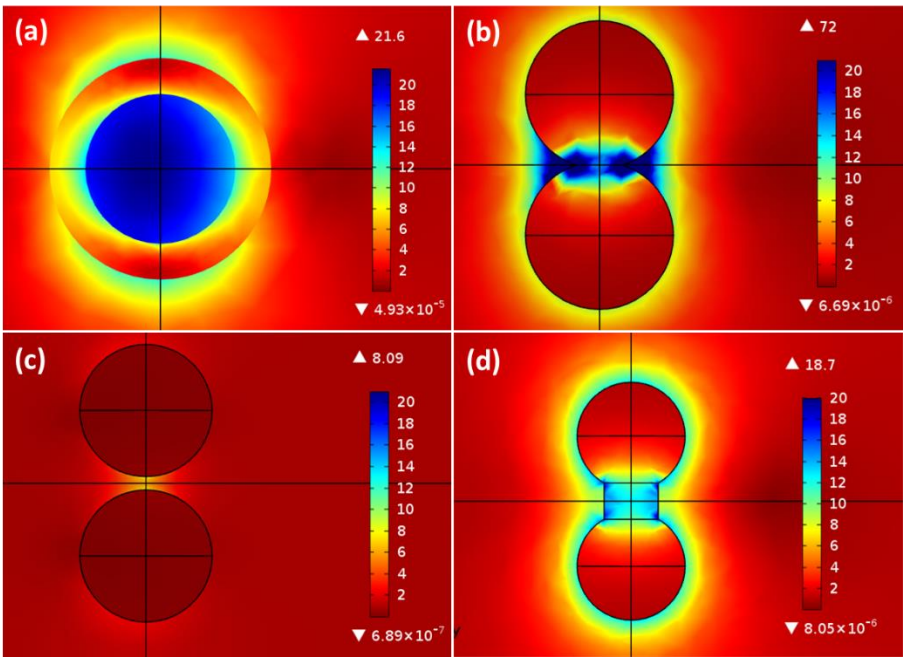


**Figure 9.** E-filed enhancement maps at the irradiation wavelength of 785. (a) Si@Au (44nm@21nm), (b) Au bi-sphere (r = 25 nm, distance 47.5nm), (c) Au bi-sphere (r = 25 nm, distance 55 nm), (d) dumbbell-like structure ($r_0$ = 13.5 nm). Δ and ∇ are maximum and minimum values of the E-filed enhancement, respectively.

Based on the results of FEM simulations and their comparison with the experimental measurements of 4-MBA SERS spectra we may conclude, that SERS-active bSi/Au substrate is very efficient for detecting biological objects as it allows to use NIR laser source for sample irradiation and provides extremely high E-field enhancement. The major mechanism in Raman signal enhancement is the local surface plasmon resonance (LSPR). Simulation results indicate that the EF due to local surface plasmon resonance reaches a value of $10^4$-$10^7$, while the experimentally obtained value of the EF is $10^8$ (expecting the remaining contribution of CM).

bSi/Au possesses a significant advantage over the conventional plane SERS-active surfaces with Au hot-spots because it enables confining the living cells and biomolecules into a 3D enclosure surrounded with the hotspots. For Au nanoparticles of the average diameter of 50 nm LSPR should appear for 500-530 nm excitation. This statement is proved both by the existing data and our simulation results (see Fig. 7). In our experiments we used 785 nm laser for excitation, thus LSPR did not take place. Living cell sample measurement was provided for only 30 s with 785 nm laser (this excitation wavelength is not resonant to lots of the living cell components such as proteins, DNA, RNA, as 532 nm [48]; however, its application is favorable as it is not damaging to cells and tissues and can provide non-destructing analysis). This time period and laser power were not enough to obtain a living cell Raman spectrum with an acceptable signal-to-noise ratio on the flat $SiO_2$/Au. But due to the increase of the bSi/Au absorption cross-section in the NIR region, the observation of the living cell SERS spectrum on them becomes possible. Moreover, the predominantly vertical orientation of the gold bi-spheres and dumbbells (see SEM images in Fig. 2) on the Si cone surface allows one to obtain an excellent enhancement of the Raman signal by employing plasmon resonance situated in the red and NIR region.

*DFT modeling: Chemical enhancement contribution to SERS*

To evaluate the enhancement of the SERS signal via the CM mechanism, we employed DFT analysis by studying the equilibrium geometry, electronic structure, and Raman spectra of the 4-MBA molecule and the complexes 4-MBA/Au. Simulated Raman and SERS spectra in comparison with experimentally obtained ones, as well as optimized geometries of 4-MBA molecule and 4-MBA/Au (insets) are presented in Fig. 10. Simulated spectra display a good agreement with the experimental results. Peak assignment of the main characteristic bands in the simulated and experimental Raman spectra of 4-MBA molecules and SERS spectra of 4-MBA/Au complexes are

summarized in Table 2. The charge transfer (CT) mechanism is a short-range effect caused by the chemical interaction between the adsorbed molecule and the metal or semiconductor surface[49]. It was shown, that the CT process leads to the symmetrical modes enhancement in general, whereas the modes involving the vibrational coordinates, which are relaxed by the electronically excited state would be enhanced preferably[50]. In our experiments, we observe a significant increase in $\nu_{12}$ ($a_1$) aromatic ring breathing mode (1077 $cm^{-1}$) and $\nu_{8a}$ ($a_1$) totally symmetric ν C-C ($a_1$) (1587 $cm^{-1}$) intensities, which is well confirmed by DFT simulations, considering chemical mechanism (molecule adsorption on the Au surface, charge transfer) impact in the Raman signal enhancement. Nevertheless, the DFT simulation results allow us to conclude that the CT process contributes to the signal enhancement by no more than one order of magnitude (supporting the primary contribution of EM mechanism as follows from FEM modeling and comparison of both contributions with the experimental observations). It has been demonstrated in [51] that for 4-Aminothiophenol molecule (it differs from 4-MBA with one functional group) adsorbed on the Au nanorings, the 1075 $cm^{-1}$ enhancement is observed only for excitation with 785 nm laser and have pure EM origin. In our study enhancement of 1075 $cm^{-1}$ and 1585 $cm^{-1}$ bands was of the same order (EF ~ $10^8$), which allows us to conclude that the contribution of the CT mechanism to SERS-enhancement of molecules adsorbed on the bSi/Au surface is negligible. Thus, when excited by a 785 nm laser, the electromagnetic mechanism of surface-enhanced Raman spectra dominates.

4-MBA molecules were covalently bonded to the Au surface. It is confirmed by the appearance of a 220 $cm^{-1}$ band of Au-S and the absence of a 2565 $cm^{-1}$ band of S-H (see Fig. 3S, Supplementary Information). According to the procedure of the molecular monolayer formation and data, presented in [52], we suppose vertical configuration of the molecules on the bSi/Au substrate. 4-MBA molecules flat orientation to the surface could be identified by strong out-of-

plane γ(CCC) vibration of the aromatic ring. In the SERS spectrum of 4-MBA molecules on bSi/Au surface this band at 713 $cm^{-1}$ responsible for γ(CCC) as well as 848 $cm^{-1}$ corresponding to β($COO^-$) are practically vanished, while 1706 $cm^{-1}$ corresponding to C=O stretching vibrations of non-dissociated COOH groups is present. These experimental data are in good agreement with the results of DFT calculations (no γ(CCC) and β($COO^-$) bands, while C=O at 1713 $cm^{-1}$ is present, see Table 2 and Fig. 10) and confirm the vertical orientation of the 4-MBA molecules on the bSi/Au substrate [52].

The appearance of a band 848 $cm^{-1}$, assigned to the $COO^-$ stretching mode, in the SERS spectrum likely indicates that some 4-MBA molecules are deprotonated. $pK_a$ of the 4-MBA is 4.2 for free 4-MBA and 5.6 for covalent band to gold nanoparticles [36]. At pH 7 4-MBA is totally deprotonated [53] as ethanol pH value 7.33. During samples drying procedure in the presence of humid air the 4-MBA molecules protonation via hydration. However, a small part of them remained deprotonated, as we observe due to the 848 $cm^{-1}$ band.

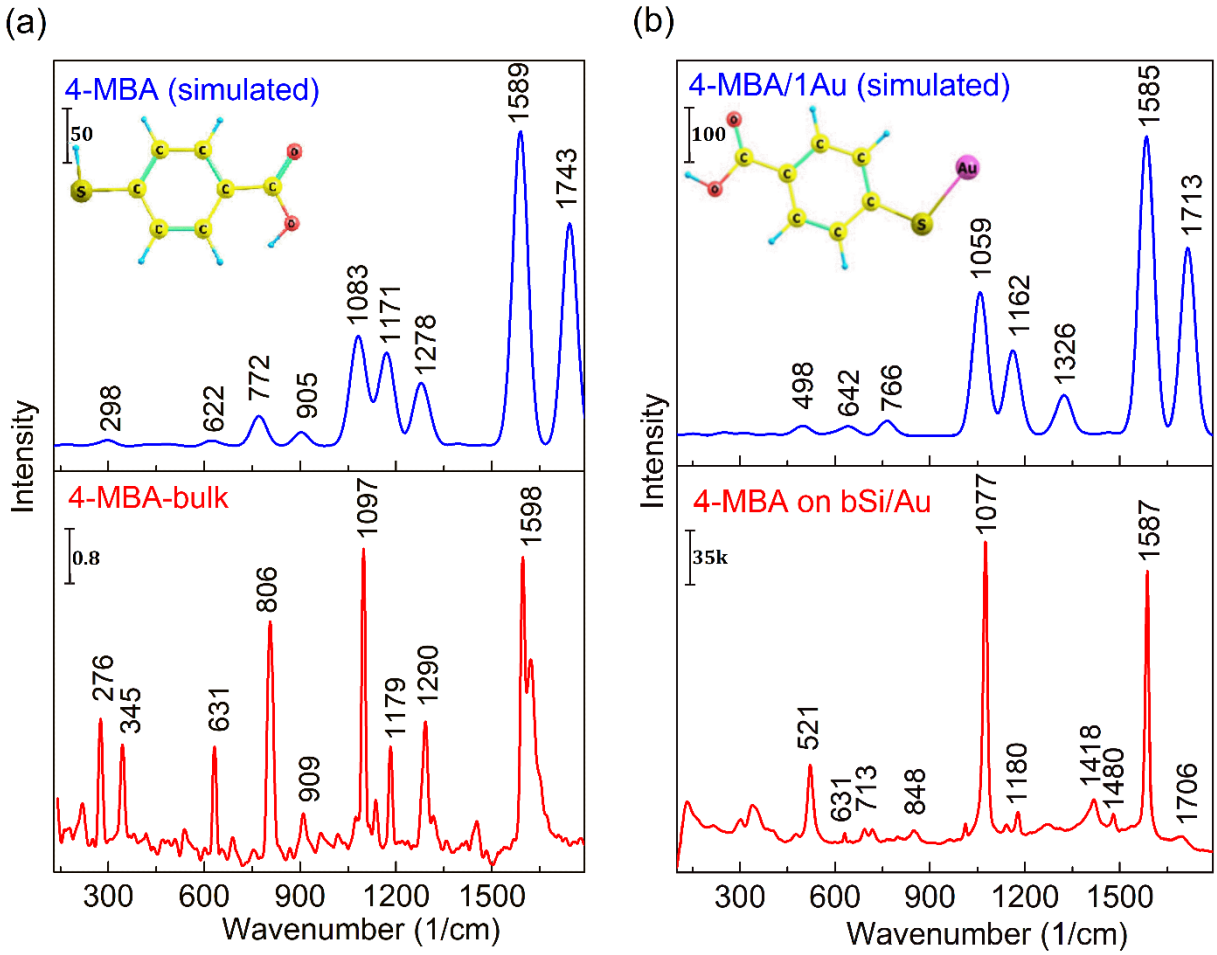


**Figure 10.** Simulated and experimental Raman spectra of 4-MBA molecules (a) and SERS spectra of 4-MBA/Au complexes (b) with optimized geometries of 4-MBA molecule and 4-MBA/Au complex (insets in (a) and (b), respectively). Intensity is presented in arbitrary units as a scale bar. Simulated vibrational bands were fitted with Gaussian profile with a bandwidth of 30 $cm^{-1}$.

**Table 2.** Peak assignment of the main characteristic bands in the simulated and experimental Raman spectra of 4-MBA molecules and SERS spectra of 4-MBA/Au complexes

| 4-MBA {exp.} ($cm^{-1}$) | 4-MBA {theor.} ($cm^{-1}$) | 4-MBA on bSi/Au {exp.$^{SERS}$} ($cm^{-1}$) | 4-MBA/Au {theor.$^{SERS}$} ($cm^{-1}$) | Peak assignment |
|---|---|---|---|---|
| – | – | 521 | 498 | ν(CS) [36,54] |

| | | | | |
|---|---|---|---|---|
| | | | | δ(COOH) deformation |
| 631 | 622 | 631 | 642 | $\nu_{6b}$ [36] +δ( COOH) deformation |
| – | – | 693 | – | γ(CH) out-of-plane [54] |
| – | – | 713 | – | $\nu_{4b}$ + γ(CCC) out-of-plane [36,54] |
| 806 | 772 | – | 766 | $\nu_{10a}$ [36] in-plane aromatic ring breathing mode +-COH deformation |
| – | – | 848 | – | β($COO^-$) [36] |
| 909 | 905 | – | – | β(SH) [36] |
| – | – | 1013 | – | in-plane ring breathing, $b_2$ [36,49,54] |
| 1097 | 1083 | 1077 | 1059 | $\nu_{12}$ ($a_1$) in-plane aromatic ring breathing mode + ν(CS), $a_1$ [33,49,54,55,56] |
| – | – | 1142 | – | $\nu_{15}$ ($b_2$) δ(CH) deformation [33,54,56] |
| 1179 | 1171 | 1180 | 1162 | $\nu_9$ ($a_1$) δ(CH) deformation [33,36,49,55,56] |
| 1290 | 1278 | – | – | $\nu_3$ [36] |
| – | – | – | 1326 | δ(OH) deformation δ( C-Ar) deformation |
| – | – | 1418 | – | ν ($COO^-$) stretching mode [33,36,49] |
| – | – | 1480 | – | ν(CC) + γ(CH) [54,55] |
| 1598 | 1589 | 1587 | 1585 | $\nu_{8a}$ ($a_1$) totally symmetric aromatic ring vibration [33,36,49,54,55,56] |
| – | 1743 | 1706 | 1713 | ν (C=O) stretching mode |

*Note:* the vibrational modes indication ν – stretching, β – bending, δ – deformation, γ – out-of-plane deformation

## CONCLUSIONS

Detection of single organic molecules and living cells with high throughput, speed, and resolution is a very challenging biosensing task. Creating a SERS-active biosensor platform one

should aim to use NIR light for excitation, low power values to prevent possible living cell damage, as well as to minimize the signal accumulation time to acquire accurate information on dynamic biochemical and biophysical processes in living cells. Special attention must also be paid to the quality of the surfaces used for SERS of living cells, as hot spots density and EF must satisfy the requirements of uniformity, sensitivity resistance to external influences, easy low-cost reproducibility on an industrial scale.

We propose a new SERS-active platform for detection of not only trace amounts of small organic molecules, but also living cells. The developed bSi/Au substrate ensures high sensitivity by exploring nanoscale roughness of submicron regular cone structures evenly distributed over the entire surface. The increased effective surface area at dense and homogeneous hot spot distribution allows us to obtain the EF of about $10^8$. It is worth adding that the proposed SERS-active substrate requires only a 25÷50 nm gold layer instead of 100-400 nm conventionally used for $SiO_2$-based substrates thus significantly reducing production costs.

The performed numerical FEM simulation confirmed the strong enhancement of the local field at the bSi/Au surface and revealed that the outstanding performance of bSi/Au substrate originates mostly from the EM mechanism of SERS. Moreover, we demonstrate that the dominating vertical orientation of the gold bi-spheres and dumbbells along bSi/Au cones is crucial for achieving the high efficiency of the substrate in the NIR spectral range. DFT analysis exhibits a relatively small contribution of CM to the SERS activity of bSi/Au, at the level of one order of the EF magnitude vs seven orders coming from the electromagnetic enhancement.

Implementation of the bSi/Au substrate for living C6 rat glioma cell analysis made it possible to visualize the characteristic bands of nucleic acids, proteins, and lipids in the “fingerprint” SERS spectrum region with low excitation intensities and short accumulation time. Moreover, we

demonstrated that the bSi/Au substrate has tremendous potential for the real-time cellular dynamics SERS observations. Thus, the bSi/Au substrates may be easily fabricated on a large-scale using existing well-developed techniques, with the tune control of specific surface parameters, providing efficient Raman signal enhancement, stability, and reproducibility.

We demonstrate that covering of bSi with up to 50 nm thick golden layer leads to the formation of specific size-geometry hot spots to enhance the bSi-for-SERS selectivity and sensitivity.

Applying these bSi/Au substrates for SERS biochemical changes detection overcomes the limitations of other biosensing platforms and provides precise information on biochemistry of cell behavior, cell-substrate contact, metabolism. BSi/Au can be implemented for high-throughput screening due to outstanding bSi-for-SERS sensitivity and ease of use. Proposed bSi/Au substrates production fully meets the specified requirements for effective SERS of living cells and allows the scalable production of the low-cost SERS-active hydrophilic substrates of outstanding quality and reproducibility.

## METHODS

### *Materials and substrates preparation*

The silicon used in the experiment was lightly p-doped, 0.5 mm thick silicon wafers. The bSi was formed in a cryogenic, inductively coupled plasma reactive ion etcher as reported in [57], [58]. As a plain reference substrate quartz slides ($SiO_2$) were used.

Before the vacuum deposition of gold, the substrates were rinsed with ethanol for 10 minutes, washed in deionized water, and dried in a dry stream of $N_2$. The Au films were deposited on the bSi and $SiO_2$ substrates using Quorum Q150T ES Plus-Turbomolecular pumped coater. Sputtering

parameters for targets were, as follows: Au, sputter current 50 mA, sputter time 120 s, argon pressure 2 mBar.

Before surface coating with testing molecules or cells bSi/Au and $SiO_2$/Au substrates were held in $N_2$ atmosphere to prevent undesirable absorption of impurity molecules by these substrates. Both bSi/Au and $SiO_2$/Au slides were incubated in the 4-Mercaptobenzoic acid (4-MBA, $HSC_6H_4CO_2H$; Sigma, USA) solution at a final concentration $5 \cdot 10^{-3}$ mol/L for 4 hours to provide the molecular monolayer formation on the gold-covered surface of the $SiO_2$ slides and bSi through –SH group. Then all samples were washed with ethanol flow for 10 min to remove the trace amounts of 4-MBA molecules not bounded to the surface, dried with $N_2$, and kept in hermetically closed containers before SERS measurements. For SERS of living cells prepared bSi/Au and $SiO_2$/Au substrates were additionally sterilized at 110°C for 2 h and then in full sterility placed in plastic Petri dishes in cell culture medium DMEM/F12.

*Cell culture*

ATCC C6 (ATCC ® CCL-107 ™) rat glioma cells were obtained from ATCC, LGC Standards, Ogrodowa 27/29, Kielpin, Poland, and used in all experiments. DMEM/F12 medium (Gibco) supplemented with 10% fetal bovine serum (Sigma) and 80 μg/mL gentamycin sulfate (Belmedpreparaty, Belarus) were used for cell growth. C6 glioma cells were held in 100% humidity at 37°C in 5% $CO_2$ atmosphere. In the log-phase cells were trypsinized, centrifuged at 1500 rpm, and $10^5$ cells were seeded in standard 3.5 cm plastic Petri dishes with bSi/Au or $SiO_2$/Au slides placed on the Petri dish bottom. Cells were cultured for 3 days and all measurements were conducted at 70% cell confluence. To exclude undesirable SERS signal from growth medium components during measurements it was replaced by Hepes buffer solution (pH 7.2) of the

following content (in mmol/L): NaCl – 131, KCl – 5, $MgSO_4$ – 1.3, $CaCl_2$ – 1.3, Hepes – 20, $C_6H_{12}O_6$ – 5.

*Fluorescence microscopy*

Fluorescence images were recorded using a fluorescence microscope built around an inverted biological Nikon Eclipse Ti-U with a 40× CFI S Plan Fluor ELWD air objective and operated in the wide-field epi-illumination mode. The excitation source was 532 nm CW DPSS laser (Crystalaser). The excitation spot diameter was about 200 μm. The laser power after the objective was 60 μW. The excitation laser was focused into the back focal plane of the objective with a 600 mm focal distance achromatic doublet and directed into the objective by a 50/50 beam splitter. The resulting fluorescence was filtered off the excitation light with the long-pass filter (HQ545LP, Chroma) and imaged with EMCCD (DU-897E-CS0-UVB, Andor). The camera EM gain was 150, the integration time was 0.1 s and each image was an average of 20 frames.

*Cell viability detection*

Viability determination was performed via Propidium Iodide (PI) assay. PI is a cell membrane non-penetrating fluorescent dye, which becomes strongly fluorescent only if in penetrates the cell membrane and intercalate in DNA molecules. Cells on the bSi/Au substrate were washed twice with Hepes-buffer, fluorescence measurements were conducted in Hepes-buffer containing $10^{-6}$ M of PI.

Cell death control study was performed by cell permeabilization and fixation with ice-cold ethanol: cell culture medium was removed, cells on the bSi/Au substrates were gently washed with Hepes-buffer, the sample was immersed in ice-cold ethanol and stored at 4 ºC for 30 minutes. Then the sample was washed twice with Hepes-buffer, and ones with distilled water. Measurements were conducted in medium containing $10^{-6}$ M of PI.

*SEM, TEM and image processing*

Scanning electron microscopy (SEM) micrographs of investigated samples were obtained by Helios NanoLab 650 model microscope, manufactured by FEI. Analysis of bSi and bSi/Au was performed with a nominal beam voltage of 3 kV. Transmission electron microscopy (TEM) was performed with transmission electron microscope Tecnai G2 F20 X-TWIN (FEI, Netherlands, 2011) with the Schottky type field emission electron source.

The bSi surface dimensions were tracked and analyzed manually by open-source software ImageJ (https://imagej.nih.gov/ij/). Surface dimensions are presented as mean±SD.

*SERS*

Raman spectra measurements were obtained using the inVia confocal microscopic Raman system (Renishaw) with the 785-nm beam of the diode laser used as the excitation source. The laser power at the samples was restricted to 10 μW for 4-MBA observations (air Objective 50x) and 10 mW for living cell spectra detection. Such power increase for living cells is associated with the measurement conditions and intended to overcome power dissipation and signal loss: living cells were investigated in Petri dishes with 0.5 cm of liquid Hepes-buffer solution above the cells, causing some radiation absorption by water in NIR, and with air Objective 20x. The excitation wavelength 785 nm belongs to the tissue optical window and is not damaging to cells and tissues. Irradiation of living cells with the wavelength of 488 and 514.5 nm with only 5 mW laser power leads to cell overheating and death, but 115 mW power of 785 nm irradiation for more than 1 h does not influence cell viability [39]. The exposure time was 10s and the spectra were collected 3 times to obtain a better signal-to-noise ratio. The intensity was estimated as counts per second. For spectra graphical presentation simple baseline correction was performed.

*Electromagnetic enhancement mechanism (EM) simulation*

For evaluation of the local surface plasmon resonance impact in Raman signal enhancement Au and Si/Au nanostructure models were designed using FEM based COMSOL Multiphysics 5.5 software. The simulation domain is comprised of a nanostructure with experimentally obtained geometry with an air domain surrounded by a perfectly matched layer. The wavelength-dependent optical properties such as the absorption cross-section were simulated. The substrate was excluded from the simulation to reduce computation time. Moreover, the influence of the substrate of the considered Au plasmonic structures is the higher-order effect and the aim of the simulations was to show the general tendency and to explain the observed SERS enhancement.

*Chemical mechanisms (CM) simulation*

The equilibrium geometry, electronic structure, and Raman spectra of the complexes 4-MBA-Au which simulated 4-MBA adsorption on Au, and 4-MBA molecule were simulated using non-empiric density functional theory (DFT). The calculations were carried out with the B3LYP exchange-correlation functional and mixed basis sets using computational chemistry software package Gaussian 16, Revision B.01 for structure optimization, and Raman spectra simulation of 4-MBA adsorption on Au. The basis sets for H, C, O, and S atoms were aug-cc-pvdz [59], which included the polarization function and diffuse functions to all four kinds of atoms. For the Au atom, the valence electrons and the inner shell electrons were described by the LANL2DZ basis set and the corresponding relativistic effective core potentials, respectively [60]. The chemical enhancement (CM) mechanism in SERS spectra involves the formation of new electronic states due to charge transfer (CT) or adsorbate-substrate bonding interactions [61]. B3LYP functional has the problems with resolving long-range CT processes[62]. For this reason, in order to take into account the CT effect CAM-B3LYP and B3LYP–D3 functionals were used. These functionals provide a more accurate asymptotic behavior for CT transitions. The CAM-B3LYP functional[63] is

based on the long-range correction of the exchange potential[64,65] and used the Coulomb-attenuating method (CAM). B3LYP-D3 denotes a calculation with the usual B3LYP functional and a D3 dispersion correction energy term. In this method developed by Grimme, the DFT-Dispersion method appends to the base functional a scaled, damped, and fitted leading term to the dispersion energy series[66]. Thus, in Raman spectra simulations, DFT/CAM-B3LYP/aug-cc-pvdz/LANL2DZ and DFT/ B3LYP-D3/aug-cc-pvdz/LANL2DZ levels of theory were applied. In our calculations scaling factor of 0.97 was used [67].

For the investigation of the adsorption behavior of 4-MBA on gold nanostructures, the model proposed in [68] was used, supposing 4-MBA molecule adsorption on one Au atom through the S atom with parallel orientation. Consideration of more Au atoms during the formation of a complex with a 4-MBA molecule significantly complicates the vibration spectra calculations. Thus, only Au atom was used in simulations, and as the mass of Au atom is relatively large, this makes the approximation reasonable[68].

## ASSOCIATED CONTENT

### Supporting information

Determination of the semisphere diameters; SERS-response quality control: time-dependence; laser power range test for SERS-response; hydrophilic properties of bSi/Au and plastic Petri dish comparison; glioma cells on substrates viability determination.

## NOTES

The authors declare no competing financial interest.

## AUTHOR INFORMATION

**Corresponding Author**

Lena Golubewa, Center for Physical Sciences and Technology, Sauletekio Ave. 3, LT-10257 Vilnius, Lithuania; Institute for Nuclear Problems, Belarusian State University, Bobruiskaya 11, 220030 Minsk, Belarus; lena.golubewa@ftmc.lt

**Authors**

Renata Karpicz, Center for Physical Sciences and Technology, Sauletekio Ave. 3, LT-10257 Vilnius, Lithuania; renata.karpicz@ftmc.lt

Ieva Matulaitienė, Center for Physical Sciences and Technology, Sauletekio Ave. 3, LT-10257 Vilnius, Lithuania; ieva.matulaitiene@ftmc.lt

Algirdas Selskis, Center for Physical Sciences and Technology, Sauletekio Ave. 3, LT-10257 Vilnius, Lithuania; algirdas.selskis@ftmc.lt

Danielis Rutkauskas, Center for Physical Sciences and Technology, Sauletekio Ave. 3, LT-10257 Vilnius, Lithuania; danielis@ar.fi.lt

Alexander Pushkarchuk, Institute of Physical Organic Chemistry, National Academy of Sciences of Belarus, Surganov St. 13, 220072 Minsk, Belarus; Institute for Nuclear Problems, Belarusian State University, Bobruiskaya 11, 220030 Minsk, Belarus; alexp51@bk.ru

Tatsiana Khlopina, Institute for Nuclear Problems, Belarusian State University, Bobruiskaya 11, 220030 Minsk, Belarus; tatianasvirid298@gmail.com

Dominik Michels, Computer, Electrical and Mathematical Science and Engineering Division, 4700 King Abdullah University of Science and Technology, Thuwal 23955-6900, Saudi Arabia; dominik.michels@kaust.edu.sa

Dmitry Lyakhov, Computer, Electrical and Mathematical Science and Engineering Division, 4700 King Abdullah University of Science and Technology, Thuwal 23955-6900, Saudi Arabia; dmitry.lyakhov@kaust.edu.sa

Tatsiana Kulahava, Institute for Nuclear Problems, Belarusian State University, Bobruiskaya 11, 220030 Minsk, Belarus; tatyana_kulagova@tut.by

Ali Shah, Department of Micro and Nanosciences, Aalto University, Espoo, P.O. Box 13500, FI-00076, Finland; ali.shah07@outlook.com

Yuri Svirko, Institute of Photonics, University of Eastern Finland, Yliopistokatu 2, FI-80100 Joensuu, Finland; yuri.svirko@uef.fi

Polina Kuzhir, Institute of Photonics, University of Eastern Finland, Yliopistokatu 2, FI-80100 Joensuu, Finland; Institute for Nuclear Problems, Belarusian State University, Bobruiskaya 11, 220030 Minsk, Belarus; polina.kuzhir@uef.fi

## ACKNOWLEDGEMENTS

This work was supported by Horizon 2020 RISE DiSeTCom Project 823728, the Academy of Finland (projects nos. 320166 and 298298), joint project no. S-LB-19-4 from the Research Council of Lithuania Foundation, the Belarusian Republican Foundation for Fundamental Research (BRFFR) project F19LITG-003. P.P.K. is supported by Horizon 2020 IF TURANDOT project 836816. The authors are grateful to Dr. Martynas Skapas and Mr Martynas Talaikis (Center for Physical Sciences and Technology, Vilnius, Lithuania) for assistance in TEM and Raman measurements, respectively, and to Alesia Paddubskaya (Institute for Nuclear Problems, Belarusian State University, Minsk, Belarus) for valuable discussions and interest to the work.

ABBREVIATIONS

UV, ultraviolet; NIR, near-infrared; SERS, surface-enhanced Raman spectroscopy; bSi, black silicon; EF, enhancement factor; E-field, electromagnetic field; EM, electromagnetic mechanism; CM, chemical mechanism; CT, charge transfer; FEM, finite element method; DFT, density functional theory; SEM, scanning electron microscopy; TEM, transmission electron microscopy; 4-MBA, 4-mercaptobenzoic acid; LSPR, local surface plasmon resonance; GSH, glutathione, reduced state; GSSG, glutathione, oxidized state; PI, propidium iodide.

REFERENCES

(1) Bhalla, N.; Jolly, P.; Formisano, N.; Estrela, P. Introduction to Biosensors. *Essays Biochem.* **2016**, *60* (1), 1–8. https://doi.org/10.1042/EBC20150001.

(2) Sato, H.; Ishigaki, M.; Taketani, A.; Andriana, B. B. Raman Spectroscopy and Its Use for Live Cell and Tissue Analysis. *Biomed. Spectrosc. Imaging* **2019**, *7* (3–4), 97–104. https://doi.org/10.3233/bsi-180184.

(3) Smith, R.; Wright, K. L.; Ashton, L. Raman Spectroscopy: An Evolving Technique for Live Cell Studies. *Analyst* **2016**, *141* (12), 3590–3600. https://doi.org/10.1039/c6an00152a.

(4) Notingher, I. Raman Spectroscopy Cell-Based Biosensors. *Sensors* **2007**, *7* (8), 1343–1358. https://doi.org/10.3390/s7081343.

(5) Cialla, D.; Pollok, S.; Steinbrücker, C.; Weber, K.; Popp, J. SERS-Based Detection of Biomolecules. *Nanophotonics* **2014**, *3* (6), 383–411. https://doi.org/10.1515/nanoph-2013-0024.

(6) Jia, M.; Li, S.; Zang, L.; Lu, X.; Zhang, H. Analysis of Biomolecules Based on the Surface

Enhanced Raman Spectroscopy. *Nanomaterials*. MDPI AG September 15, 2018. https://doi.org/10.3390/nano8090730.

(7) Xu, F.; Ma, F.; Ding, Z.; Xiao, L.; Zhang, X.; Lu, Q.; Lu, G.; Kaplan, D. L. SERS Substrate with Silk Nanoribbons as Interlayer Template. *ACS Appl. Mater. Interfaces* **2019**, *11* (46), 42896–42903. https://doi.org/10.1021/acsami.9b13543.

(8) Han, G.; Liu, R.; Han, M. Y.; Jiang, C.; Wang, J.; Du, S.; Liu, B.; Zhang, Z. Label-Free Surface-Enhanced Raman Scattering Imaging to Monitor the Metabolism of Antitumor Drug 6-Mercaptopurine in Living Cells. *Anal. Chem.* **2014**, *86* (23), 11503–11507. https://doi.org/10.1021/ac503539w.

(9) Veloso, A. B.; Longo, J. P. F.; Muehlmann, L. A.; Tollstadius, B. F.; Souza, P. E. N.; Azevedo, R. B.; Morais, P. C.; Da Silva, S. W. SERS Investigation of Cancer Cells Treated with PDT: Quantification of Cell Survival and Follow-Up. *Sci. Rep.* **2017**, *7* (1), 1–12. https://doi.org/10.1038/s41598-017-07469-1.

(10) Fraire, J. C.; Stremersch, S.; Bouckaert, D.; Monteyne, T.; De Beer, T.; Wuytens, P.; De Rycke, R.; Skirtach, A. G.; Raemdonck, K.; De Smedt, S.; Braeckmans, K. Improved Label-Free Identification of Individual Exosome-like Vesicles with Au@Ag Nanoparticles as SERS Substrate. *ACS Appl. Mater. Interfaces* **2019**, *11* (43), 39424–39435. https://doi.org/10.1021/acsami.9b11473.

(11) Panikkanvalappil, S. R.; Hira, S. M.; El-Sayed, M. A. Elucidation of Ultraviolet Radiation-Induced Cell Responses and Intracellular Biomolecular Dynamics in Mammalian Cells Using Surface-Enhanced Raman Spectroscopy. *Chem. Sci.* **2016**, *7* (2), 1133–1141. https://doi.org/10.1039/c5sc03817k.

(12) Leong, S. X.; Koh, L. K.; Koh, C. S. L.; Phan-Quang, G. C.; Lee, H. K.; Ling, X. Y. In Situ Differentiation of Multiplex Noncovalent Interactions Using SERS and Chemometrics. *ACS Appl. Mater. Interfaces* **2020**, *12* (29), 33421–33427. https://doi.org/10.1021/acsami.0c08053.

(13) Kim, S.; Kim, T. G.; Lee, S. H.; Kim, W.; Bang, A.; Moon, S. W.; Song, J.; Shin, J. H.; Yu, J. S.; Choi, S. Label-Free Surface-Enhanced Raman Spectroscopy Biosensor for On-Site Breast Cancer Detection Using Human Tears. *ACS Appl. Mater. Interfaces* **2020**, *12* (7), 7897–7904. https://doi.org/10.1021/acsami.9b19421.

(14) Park, M.; Hwang, C. S. H.; Jeong, K. H. Nanoplasmonic Alloy of Au/Ag Nanocomposites on Paper Substrate for Biosensing Applications. *ACS Appl. Mater. Interfaces* **2018**, *10* (1), 290–295. https://doi.org/10.1021/acsami.7b16182.

(15) Mei, R.; Wang, Y.; Yu, Q.; Yin, Y.; Zhao, R.; Chen, L. Gold Nanorod Array-Bridged Internal-Standard SERS Tags: From Ultrasensitivity to Multifunctionality. *ACS Appl. Mater. Interfaces* **2020**, *12* (2), 2059–2066. https://doi.org/10.1021/acsami.9b18292.

(16) Tan, Y.; Gu, J.; Xu, W.; Chen, Z.; Liu, D.; Liu, Q.; Zhang, D. Reduction of CuO Butterfly Wing Scales Generates Cu SERS Substrates for DNA Base Detection. *ACS Appl. Mater. Interfaces* **2013**, *5* (20), 9878–9882. https://doi.org/10.1021/am402699c.

(17) Sitjar, J.; Liao, J. Der; Lee, H.; Liu, B. H.; Fu, W. E. SERS-Active Substrate with Collective Amplification Design for Trace Analysis of Pesticides. *Nanomaterials* **2019**, *9* (5), 1–12. https://doi.org/10.3390/nano9050664.

(18) Shiohara, A.; Wang, Y.; Liz-Marzán, L. M. Recent Approaches toward Creation of Hot

Spots for SERS Detection. *J. Photochem. Photobiol. C Photochem. Rev.* **2014**, *21*, 2–25. https://doi.org/10.1016/j.jphotochemrev.2014.09.001.

(19) Yao, X.; Jiang, S.; Luo, S.; Liu, B. W.; Huang, T. X.; Hu, S.; Zhu, J.; Wang, X.; Ren, B. Uniform Periodic Bowtie SERS Substrate with Narrow Nanogaps Obtained by Monitored Pulsed Electrodeposition. *ACS Appl. Mater. Interfaces* **2020**, *12* (32), 36505–36512. https://doi.org/10.1021/acsami.0c09357.

(20) Hajduková, N.; Procházka, M.; Štěpánek, J.; Špírková, M. Chemically Reduced and Laser-Ablated Gold Nanoparticles Immobilized to Silanized Glass Plates: Preparation, Characterization and SERS Spectral Testing. *Colloids Surfaces A Physicochem. Eng. Asp.* **2007**, *301* (1–3), 264–270. https://doi.org/10.1016/j.colsurfa.2006.12.065.

(21) Fan, M.; Andrade, G. F. S.; Brolo, A. G. A Review on the Fabrication of Substrates for Surface Enhanced Raman Spectroscopy and Their Applications in Analytical Chemistry. *Analytica Chimica Acta*. 2011, pp 7–25. https://doi.org/10.1016/j.aca.2011.03.002.

(22) Serpenguzel, A. Luminescence of Black Silicon. *J. Nanophotonics* **2008**, *2* (1), 021770. https://doi.org/10.1117/1.2896069.

(23) Ozturk, S.; Kayabasi, E.; Kucukdogan, N.; Ayakdas, O. Progress in Applications of Black Silicon. *Most Recent Stud. Sci. Art* **2018**, *2* (April), 1866–1882.

(24) Hsu, C. H.; Wu, J. R.; Lu, Y. T.; Flood, D. J.; Barron, A. R.; Chen, L. C. Fabrication and Characteristics of Black Silicon for Solar Cell Applications: An Overview. *Materials Science in Semiconductor Processing*. Elsevier Ltd September 1, 2014, pp 2–17. https://doi.org/10.1016/j.mssp.2014.02.005.

(25) Hoyer, P.; Theuer, M.; Beigang, R.; Kley, E. B. Terahertz Emission from Black Silicon. *Appl. Phys. Lett.* **2008**, *93* (9), 091106. https://doi.org/10.1063/1.2978096.

(26) Wang, X.; Bhadra, C. M.; Yen Dang, T. H.; Buividas, R.; Wang, J.; Crawford, R. J.; Ivanova, E. P.; Juodkazis, S. A Bactericidal Microfluidic Device Constructed Using Nano-Textured Black Silicon. *RSC Adv.* **2016**, *6* (31), 26300–26306. https://doi.org/10.1039/c6ra03864f.

(27) Liu, X. L.; Zhu, S. W.; Sun, H. Bin; Hu, Y.; Ma, S. X.; Ning, X. J.; Zhao, L.; Zhuang, J. "infinite Sensitivity" of Black Silicon Ammonia Sensor Achieved by Optical and Electric Dual Drives. *ACS Appl. Mater. Interfaces* **2018**, *10* (5), 5061–5071. https://doi.org/10.1021/acsami.7b16542.

(28) Mironenko, A. Y.; Tutov, M. V.; Sergeev, A. A.; Mitsai, E. V.; Ustinov, A. Y.; Zhizhchenko, A. Y.; Linklater, D. P.; Bratskaya, S. Y.; Juodkazis, S.; Kuchmizhak, A. A. Ultratrace Nitroaromatic Vapor Detection via Surface-Enhanced Fluorescence on Carbazole-Terminated Black Silicon. *ACS Sensors* **2019**, *4* (11), 2879–2884. https://doi.org/10.1021/acssensors.9b01063.

(29) Ivanova, E. P.; Hasan, J.; Webb, H. K.; Gervinskas, G.; Juodkazis, S.; Truong, V. K.; Wu, A. H. F.; Lamb, R. N.; Baulin, V. A.; Watson, G. S.; Watson, J. A.; Mainwaring, D. E.; Crawford, R. J. Bactericidal Activity of Black Silicon. *Nat. Commun.* **2013**, *4* (1), 1–7. https://doi.org/10.1038/ncomms3838.

(30) Singh, J.; Jadhav, S.; Avasthi, S.; Sen, P. Designing Photocatalytic Nanostructured Antibacterial Surfaces: Why Is Black Silica Better than Black Silicon? *ACS Appl. Mater. Interfaces* **2020**, *12* (18), 20202–20213. https://doi.org/10.1021/acsami.0c02854.

(31) Deng, Y. L.; Juang, Y. J. Black Silicon SERS Substrate: Effect of Surface Morphology on SERS Detection and Application of Single Algal Cell Analysis. *Biosens. Bioelectron.* **2014**, *53*, 37–42. https://doi.org/10.1016/j.bios.2013.09.032.

(32) Gervinskas, G.; Seniutinas, G.; Hartley, J. S.; Kandasamy, S.; Stoddart, P. R.; Fahim, N. F.; Juodkazis, S. Surface-Enhanced Raman Scattering Sensing on Black Silicon. *Ann. Phys.* **2013**, *525* (12), 907–914. https://doi.org/10.1002/andp.201300035.

(33) Jiang, L.; You, T.; Yin, P.; Shang, Y.; Zhang, D.; Guo, L.; Yang, S. Surface-Enhanced Raman Scattering Spectra of Adsorbates on Cu2O Nanospheres: Charge-Transfer and Electromagnetic Enhancement. *Nanoscale* **2013**, *5* (7), 2784–2789. https://doi.org/10.1039/c3nr33502j.

(34) Le Ru, E. C.; Etchegoin, P. G. *Principles of Surface-Enhanced Raman Spectroscopy*; Elsevier, 2009. https://doi.org/10.1016/B978-0-444-52779-0.X0001-3.

(35) Golubewa, L.; Rehman, H.; Kulahava, T.; Karpicz, R.; Baah, M.; Kaplas, T.; Shah, A.; Malykhin, S.; Obraztsov, A.; Rutkauskas, D.; Jankunec, M.; Matulaitienė, I.; Selskis, A.; Denisov, A.; Svirko, Y.; Kuzhir, P. Macro-, Micro-and Nano-Roughness of Carbon-Based Interface with the Living Cells: Towards a Versatile Bio-Sensing Platform. *Sensors (Switzerland)* **2020**, *20* (18), 1–14. https://doi.org/10.3390/s20185028.

(36) Capocefalo, A.; Mammucari, D.; Brasili, F.; Fasolato, C.; Bordi, F.; Postorino, P.; Domenici, F. Exploring the Potentiality of a SERS-Active PH Nano-Biosensor. *Front. Chem.* **2019**, *7* (June), 1–11. https://doi.org/10.3389/fchem.2019.00413.

(37) Orendorff, C. J.; Gole, A.; Sau, T. K.; Murphy, C. J. Surface-Enhanced Raman

Spectroscopy of Self-Assembled Monolayers: Sandwich Architecture and Nanoparticle Shape Dependence. *Anal. Chem.* **2005**, *77* (10), 3261–3266. https://doi.org/10.1021/ac048176x.

(38) Wu, K.; Rindzevicius, T.; Schmidt, M. S.; Mogensen, K. B.; Xiao, S.; Boisen, A. Plasmon Resonances of Ag Capped Si Nanopillars Fabricated Using Mask-Less Lithography. *Opt. Express* **2015**, *23* (10), 12965. https://doi.org/10.1364/oe.23.012965.

(39) Downes, A.; Elfick, A. Raman Spectroscopy and Related Techniques in Biomedicine. *Sensors*. Molecular Diversity Preservation International March 9, 2010, pp 1871–1889. https://doi.org/10.3390/s100301871.

(40) Shipp, D. W.; Sinjab, F.; Notingher, I. Raman Spectroscopy: Techniques and Applications in the Life Sciences. *Adv. Opt. Photonics* **2017**, *9* (2), 315. https://doi.org/10.1364/aop.9.000315.

(41) Zimmermann, A.; Zimmermann, A. Nucleus, Nuclear Structure, and Nuclear Functional Changes in Liver Cancer. In *Tumors and Tumor-Like Lesions of the Hepatobiliary Tract*; Springer International Publishing, 2017; pp 3043–3069. https://doi.org/10.1007/978-3-319-26956-6_169.

(42) Abramczyk, H.; Surmacki, J.; Kopeć, M.; Olejnik, A. K.; Lubecka-Pietruszewska, K.; Fabianowska-Majewska, K. The Role of Lipid Droplets and Adipocytes in Cancer. Raman Imaging of Cell Cultures: MCF10A, MCF7, and MDA-MB-231 Compared to Adipocytes in Cancerous Human Breast Tissue. *Analyst* **2015**, *140* (7), 2224–2235. https://doi.org/10.1039/c4an01875c.

(43) Desideri, E.; Ciccarone, F.; Ciriolo, M. R. Targeting Glutathione Metabolism: Partner in Crime in Anticancer Therapy. *Nutrients*. MDPI AG August 1, 2019. https://doi.org/10.3390/nu11081926.

(44) Kreysing, E.; Hassani, H.; Hampe, N.; Offenhäusser, A. Nanometer-Resolved Mapping of Cell-Substrate Distances of Contracting Cardiomyocytes Using Surface Plasmon Resonance Microscopy. *ACS Nano* **2018**, *12* (9), 8934–8942. https://doi.org/10.1021/acsnano.8b01396.

(45) Giebel, K. F.; Bechinger, C.; Herminghaus, S.; Riedel, M.; Leiderer, P.; Weiland, U.; Bastmeyer, M. Imaging of Cell/Substrate Contacts of Living Cells with Surface Plasmon Resonance Microscopy. *Biophys. J.* **1999**, *76* (1 I), 509–516. https://doi.org/10.1016/S0006-3495(99)77219-X.

(46) Kurouski, D.; Postiglione, T.; Deckert-Gaudig, T.; Deckert, V.; Lednev, I. K. Amide i Vibrational Mode Suppression in Surface (SERS) and Tip (TERS) Enhanced Raman Spectra of Protein Specimens. *Analyst* **2013**, *138* (6), 1665–1673. https://doi.org/10.1039/c2an36478f.

(47) Djuris, A. B.; Elazar, J. M.; Majewski, M. L. Optical Properties of Metallic Films for Vertical-Cavity Optoelectronic Devices. *Appl. Opt.* **1998**, *37* (22), 5271–5283.

(48) Brozek-Pluska, B.; Miazek, K.; Musiał, J.; Kordek, R. Label-Free Diagnostics and Cancer Surgery Raman Spectra Guidance for the Human Colon at Different Excitation Wavelengths. *RSC Adv.* **2019**, *9* (69), 40445–40454. https://doi.org/10.1039/c9ra06831g.

(49) Zhang, X. Y.; Han, D.; Pang, Z.; Sun, Y.; Wang, Y.; Zhang, Y.; Yang, J.; Chen, L. Charge

Transfer in an Ordered Ag/Cu2S/4-MBA System Based on Surface-Enhanced Raman Scattering. *J. Phys. Chem. C* **2018**, *122* (10), 5599–5605. https://doi.org/10.1021/acs.jpcc.8b00701.

(50) Brolo, A. G.; Irish, D. E.; Smith, B. D. Applications of Surface Enhanced Raman Scattering to the Study of Metal-Adsorbate Interactions. *J. Mol. Struct.* **1997**, *405* (1), 29–44. https://doi.org/10.1016/S0022-2860(96)09426-4.

(51) Ye, J.; Hutchison, J. A.; Uji-i, H.; Hofkens, J.; Lagae, L.; Maes, G.; Borghs, G.; Van Dorpe, P. Excitation Wavelength Dependent Surface Enhanced Raman Scattering of 4-Aminothiophenol on Gold Nanorings. *Nanoscale* **2012**, *4* (5), 1606. https://doi.org/10.1039/c2nr11805j.

(52) Michota, A.; Bukowska, J. Surface-Enhanced Raman Scattering (SERS) of 4-Mercaptobenzoic Acid on Silver and Gold Substrates. *J. Raman Spectrosc.* **2003**, *34* (1), 21–25. https://doi.org/10.1002/jrs.928.

(53) Phan, H. T.; Haes, A. J. Impacts of PH and Intermolecular Interactions on Surface-Enhanced Raman Scattering Chemical Enhancements. *J. Phys. Chem. C* **2018**, *122* (26), 14846–14856. https://doi.org/10.1021/acs.jpcc.8b04019.

(54) Chen, L.; Sun, H.; Zhao, Y.; Zhang, Y.; Wang, Y.; Liu, Y.; Zhang, X.; Jiang, Y.; Hua, Z.; Yang, J. Plasmonic-Induced SERS Enhancement of Shell-Dependent Ag@Cu2O Core-Shell Nanoparticles. *RSC Adv.* **2017**, *7* (27), 16553–16560. https://doi.org/10.1039/c7ra01187c.

(55) Zhu, S.; Fan, C.; Wang, J.; He, J.; Liang, E.; Chao, M. Realization of High Sensitive SERS

Substrates with One-Pot Fabrication of Ag-Fe3O4 Nanocomposites. *J. Colloid Interface Sci.* **2015**, *438*, 116–121. https://doi.org/10.1016/j.jcis.2014.09.015.

(56) Yang, L.; Jiang, X.; Ruan, W.; Yang, J.; Zhao, B.; Xu, W.; Lombardi, J. R. Charge-Transfer-Induced Surface-Enhanced Raman Scattering on Ag-TiO 2 Nanocomposites. *J. Phys. Chem. C* **2009**, *113* (36), 16226–16231. https://doi.org/10.1021/jp903600r.

(57) Sainiemi, L.; Jokinen, V.; Shah, A.; Shpak, M.; Aura, S.; Suvanto, P.; Franssila, S. Non-Reflecting Silicon and Polymer Surfaces by Plasma Etching and Replication. *Adv. Mater.* **2011**, *23* (1), 122–126. https://doi.org/10.1002/adma.201001810.

(58) Shah, A.; Stenberg, P.; Karvonen, L.; Ali, R.; Honkanen, S.; Lipsanen, H.; Peyghambarian, N.; Kuittinen, M.; Svirko, Y.; Kaplas, T. Pyrolytic Carbon Coated Black Silicon. *Sci. Rep.* **2016**, *6* (May), 10–15. https://doi.org/10.1038/srep25922.

(59) Wilson, A. K.; Van Mourik, T.; Dunning, T. H. Gaussian Basis Sets for Use in Correlated Molecular Calculations. VI. Sextuple Zeta Correlation Consistent Basis Sets for Boron through Neon. *J. Mol. Struct. THEOCHEM* **1996**, *388* (1–3), 339–349. https://doi.org/10.1016/s0166-1280(96)80048-0.

(60) Hay, P. J.; Wadt, W. R. Ab Initio Effective Core Potentials for Molecular Calculations. Potentials for K to Au Including the Outermost Core Orbitale. *J. Chem. Phys.* **1985**, *82* (1), 299–310. https://doi.org/10.1063/1.448975.

(61) Ho, C. H.; Lee, S. SERS and DFT Investigation of the Adsorption Behavior of 4-Mercaptobenzoic Acid on Silver Colloids. *Colloids Surfaces A Physicochem. Eng. Asp.* **2015**, *474*, 29–35. https://doi.org/10.1016/j.colsurfa.2015.03.004.

(62) Dreuw, A.; Head-Gordon, M. Single-Reference Ab Initio Methods for the Calculation of Excited States of Large Molecules. *Chemical Reviews*. American Chemical Society November 2005, pp 4009–4037. https://doi.org/10.1021/cr0505627.

(63) Yanai, T.; Tew, D. P.; Handy, N. C. A New Hybrid Exchange-Correlation Functional Using the Coulomb-Attenuating Method (CAM-B3LYP). *Chem. Phys. Lett.* **2004**, *393* (1–3), 51–57. https://doi.org/10.1016/j.cplett.2004.06.011.

(64) Tawada, Y.; Tsuneda, T.; Yanagisawa, S.; Yanai, T.; Hirao, K. A Long-Range-Corrected Time-Dependent Density Functional Theory. *J. Chem. Phys.* **2004**, *120* (18), 8425–8433. https://doi.org/10.1063/1.1688752.

(65) Becke, A. D. Density-Functional Thermochemistry. III. The Role of Exact Exchange. *J. Chem. Phys.* **1993**, *98* (7), 5648–5652. https://doi.org/10.1063/1.464913.

(66) Grimme, S.; Ehrlich, S.; Goerigk, L. Effect of the Damping Function in Dispersion Corrected Density Functional Theory. *J. Comput. Chem.* **2011**, *32* (7), 1456–1465. https://doi.org/10.1002/jcc.21759.

(67) Russell D. Johnson III. NIST Computational Chemistry Comparison and Benchmark Database https://cccbdb.nist.gov/intro.asp (accessed Sep 26, 2020).

(68) Ma, W. Q.; Fang, Y.; Hao, G. L.; Wang, W. G. Adsorption Behaviors of 4-Mercaptobenzoic Acid on Silver and Gold Films. *Chinese J. Chem. Phys.* **2010**, *23* (6), 659–663. https://doi.org/10.1088/1674-0068/23/06/659-663.

For Table of Contents Only